Available online at www.sciencedirect.com
ScienceDirect
Comput. Methods Appl. Mech. Engrg. 414 (2023) 116166
Computer methods in applied mechanics and engineering
www.elsevier.com/locate/cma

Pore-scale model of freezing inception in a porous medium

Alexandr Žák[a], Michal Beneš[a,*], Tissa H. Illangasekare[b]

[a] Department of Mathematics, Faculty of Nuclear Sciences and Physical Engineering, Czech Technical University in Prague, Trojanova 13, 120 00, Prague, Czech Republic
[b] Center for Experimental Study of Subsurface Environmental Processes, Colorado School of Mines, Golden, CO 80401, USA

Received 14 January 2023; received in revised form 31 May 2023; accepted 1 June 2023
Available online xxxx

Abstract

The article describes a new model of water–ice phase transition in pores of a saturated porous medium. The model takes into account the difference in specific volume between ice and water which causes structural changes in the porous medium. Describing details of heat, phase, and structure dynamics, the model contributes to a deeper understanding of phenomena in upper soil layers subjected to either seasonal conditions or climate changes. Governing multi-physics system of equations includes the conservation of mass, momentum and energy at the pore level and includes the anisotropic Allen–Cahn equation for tracking the position of ice during nucleation and growth inside the pores. The model provides space–time behavior of key quantities and describes the interaction of growing ice with pore geometry and surrounding grains. The governing system of equations is solved by the finite-element method to provide several qualitative computational studies of the ice growth inside a porous structure.

MSC: 74N20; 74F10; 76S05; 80A22

Keywords: Freezing; Thawing; Structural changes; Pore scale; Phase field; Nucleation

1. Introduction

The behavior of soil surface subjected to freezing and thawing due to seasonal dynamics or climate changes represents an interesting multi-physical topic of research coupling thermodynamics and structural changes of porous medium with applications in design and maintenance of structures (see [1,2]) in regions suffering from larger temperature variations, exploitation of oil and gas resources in cold regions (see [3]) or in leakage of methane or carbon dioxide from melting permafrost into the atmosphere (see [4,5]). Modeling such phenomena can contribute to a better understanding of climate evolution, the release of greenhouse gases, and also to progress in high-tech materials design.

Freezing and thawing in a porous medium as a heterogeneous structure involves thermal as well as structural dynamics. It is controlled by heat transfer, mostly between the soil surface and the atmosphere. The difference between the specific volume of water and ice causes expansion or shrinkage of pores, leading to displacement of grains and flow of water between them. Thin-film transport effects between ice and grains contribute to additional

* Corresponding author.
E-mail addresses: alexandr.zak@fjfi.cvut.cz (A. Žák), michal.benes@fjfi.cvut.cz (M. Beneš), tillanga@mines.edu (T.H. Illangasekare).

https://doi.org/10.1016/j.cma.2023.116166
0045-7825/

water transport. As a consequence, the porous medium expands wherever it can, mostly upwards, and creates a variety of surface patterns observable by the naked eye.

The problem of soil freezing has been studied over the last century (e.g. in [6–8]). In past decades, some more comprehensive and general approaches appeared in [5,9–11]. They use the thermodynamical principles of macroscopic poroelasticity involving constitutive relations (see [12]), or use phenomenological analogies with isothermal unsaturated porous mechanics (see [11,13,14]). The theory based on macroscopic thermodynamics incorporating a nonlinear variational approach has been established as well in [15]. Interfacial premelting and liquid films are analyzed, e.g. in [16,17]. Macroscopic thermo-hydro-mechanical modeling of frost action and frost directional penetration is contained in [18,19], ice lenses formation is simulated in [20]. Applications in real situations require careful treatment of phase transition dynamics and sometimes simplifications (as in [9,21]). As some field and experimental observations suggest (e.g. in [14,22,23]), there is a need for comprehensive theory describing the complexity of solidification processes in a porous medium.

To enhance such knowledge within the context of particular experimental evidence, a multi-physics macroscopic model of porous medium solidification with structural changes has been described in [24]. A pore-scale model considering geometrically symmetric pores in 2D has been developed in [25] whereas a general pore-scale model of freezing has been announced in [26].

In this article, we use our experience in modeling micro-scale solidification processes in material science (see, e.g. [27–31]), incorporate anisotropy and solid-phase expansion into the elementary phase transition, consequent structural dynamics, and consider the onset of the water–ice phase transition in a two-dimensional porous medium structure at the smallest pore scale. The Stefan problem with surface tension describing the phase transition is transformed into the phase-field model including the difference in phase-specific volumes where the position of the phases is tracked by the diffuse-interface Allen–Cahn equation. Suitable boundary conditions for the phase function correspond to the existence of a thin liquid film along grain boundaries. The mechanical behavior of the heterogeneous structure is described by the momentum conservation laws for each phase and grains. In Section 2, we summarize corresponding conservation laws for mass, momentum, and energy and provide constitutive laws for fluxes. In Section 3, we formulate the pore-scale multi-physics model weakly for treatment by the finite-element method and provide several computational studies that use the model to study the freezing dynamics within the pore-scale geometry.

2. Phase transition with structural effects

The micro-scale model of porous medium freezing and thawing with structural changes treats a saturated porous medium at the scale of several pores. The model is presented in the two-dimensional case. Without any restriction, it can be set in three-dimensional domains. The representative volume consisting of grains and pores filled by a water–ice system has sizes ranging between 1 μm and 1 mm. As the changes in the specific volume of phases produce forces leading to displacements in solid parts and flow in liquid parts, the Lagrangian coordinates are used.

A schematic cross-section of the pore structure is depicted in Fig. 1. Due to the size and shape of particular grains, the curvature of the growing solid phase is comparable to the curvature of grains. Their interaction due to surface tension causes an effective change of the temperature at which the porous medium freezes or melts (see [24] and references therein).

The position of particular phases dynamically changes due to the phase transition process and, unlike in [25] for symmetric pore geometry, it cannot be guessed from other governing quantities. Therefore, a method commonly used in material science (see [27,32,33]) known as the phase-field method is used to track the position of both phases. In subsequent sections, particular parts of the model are described in detail and coupled together.

2.1. Volume, coordinates and forces

The domain occupied by the heterogeneous structure of the porous medium under phase transition with volumic variation requires a coordinate system respecting the displacement of particular parts by forces produced by the volume changes. If $\mathbf{X}$ denotes the position of a material point in the reference frame, then its position change due to displacement at a given time t is $\mathbf{X} + \mathbf{u}(\mathbf{X}, t)$. Below, the conservation laws are formulated in a geometry corresponding to the initial Lagrangian configuration.

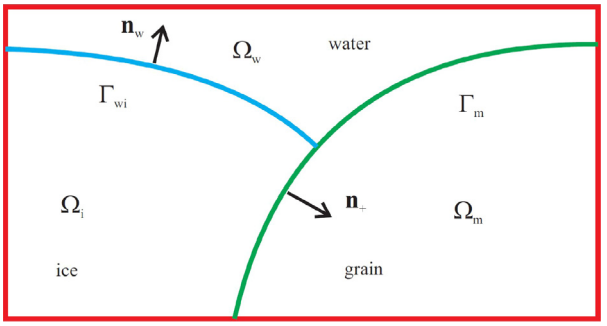

Fig. 1. Illustration of the domain with the representative volume with the grains m, water w and ice i.

Under the assumption of small deformations (compare to [25,34]), the momentum conservation law for the phase $j \in \{i, w, m\}$ is expressed as

$$\varrho_j \frac{\partial^2 \mathbf{u}_j}{\partial t^2} = \nabla \cdot \boldsymbol{\sigma}_j, \quad \text{in } \Omega_j, \quad j \in \{i, w, m\}, \tag{1}$$

where ϱ_j is the phase volumetric mass density, $\boldsymbol{\sigma}_j$ is the stress tensor and ∇ is the gradient vector with respect to the components of $\mathbf{X}$. We assume that the solid phases m, i comply with linear elasticity. Thus their stress tensors can be related to the small deformation tensor $\hat{e}$

$$\hat{e}(\mathbf{u}_j) = \frac{1}{2}(\nabla \mathbf{u}_j + (\nabla \mathbf{u}_j)^T), \quad j \in \{i, m\} \tag{2}$$

and reads as

$$\boldsymbol{\sigma}_j = \frac{E_j}{1+\nu_j}\hat{e}(\mathbf{u}_j) + \frac{\nu_j E_j \nabla \cdot \mathbf{u}_j}{(1+\nu_j)(1-2\nu_j)}\hat{I}, \quad j \in \{i, m\}, \tag{3}$$

where E_j is the Young modulus, ν_j is the Poisson ratio, and $\hat{I}$ is the unit tensor. We assume that the water phase w is a viscous Newtonian fluid characterized by the stress tensor

$$\boldsymbol{\sigma}_w = -p\hat{I} + \mu(\nabla \mathbf{v}_w + (\nabla \mathbf{v}_w)^T), \tag{4}$$

where p is the pressure, μ is the dynamic viscosity, and $\mathbf{v}_w$ is the Lagrangian water velocity.

As in [34], the equation of continuity for water as a slightly compressible fluid that reads

$$\frac{p}{\varrho_w E_w} + \nabla \cdot \mathbf{u}_w = 0, \quad \text{in } \Omega_w. \tag{5}$$

On the interfaces between ice, water and grains Γ_{wi}, Γ_{im}, Γ_{wm}, the coupling conditions of displacement and forces are described, in general, by nonlinear equations coupling the states of neighboring domains (compare with [35]). Assuming small deformations and using linearization as in [34], the mechanical coupling is through the continuity of displacement and normal forces (see also [36]).

For the intersection of three interfaces, an additional condition should be considered. At equilibrium, the Young law is commonly used to determine the contact angle of the interfaces with respect to their surface energies. In dynamical situation, the no-slip condition may lead to nonintegrable flow singularities at the contact of lines (see [37,38]). The phase-field treatment of the phase transition allows for the regularization of such singularity as indicated in [39] and therefore handles this particular issue.

2.2. Energy balance

The energy conservation in the entire system is described by the enthalpy transport equation involving the heat transfer and the latent heat release and is expressed in terms of the temperature $T = T(\mathbf{X}, t)$ which naturally is continuous across all subdomains Ω_m, Ω_i, Ω_w. Since the geometry is subject to small deformations, the enthalpy balance is linearized and formulated within the Lagrangian framework.

The conservation of energy within the subdomains Ω_m, Ω_i, Ω_w is expressed as

$$\varrho_j c_j \partial_t T + \nabla \cdot \mathbf{q}_j = 0, \quad j \in \{w, i, m\}, \tag{6}$$

where c_j is the specific heat capacity and $\mathbf{q}_j$ is the heat flux.

Coupling conditions on the interfaces between ice and grain as well as between water and grain are given by continuity of temperature and normal heat flux

$$\begin{aligned} &T|_m = T|_w, \quad \mathbf{n}_{\partial\Omega_m} \cdot \mathbf{q}_m|_m = \mathbf{n}_{\partial\Omega_m} \cdot \mathbf{q}_w|_w \quad \text{on } \Gamma_{wm}, \\ &T|_m = T|_i, \quad \mathbf{n}_{\partial\Omega_m} \cdot \mathbf{q}_m|_m = \mathbf{n}_{\partial\Omega_m} \cdot \mathbf{q}_i|_i \quad \text{on } \Gamma_{im}. \end{aligned} \tag{7}$$

On the ice–water interface Γ_{wi}, the first-order phase transition occurs where the specific latent heat l_m is being absorbed or released. This is described by the conditions on this interface

$$\begin{aligned} &T|_i = T|_w, \\ &\mathbf{n}_{\Gamma_{wi}} \cdot \mathbf{q}_i|_i - \mathbf{n}_{\Gamma_{wi}} \cdot \mathbf{q}_w|_w = \varrho_i l_m v_{\Gamma_{wi}} \quad \text{on } \Gamma_{wi}. \end{aligned} \tag{8}$$

The second condition in (8) is known as the Stefan condition. It couples the jump in heat flux across Γ_{wi} to the Lagrangian normal velocity $v_{\Gamma_{wi}}$ of the interface through the specific latent heat l_m. The role of this condition is discussed e.g. in [40,41].

The conservation law (6) is accompanied by the constitutive expression for the heat flux in the form of the linear Fourier law

$$\mathbf{q}_j = -k_j \nabla T, \quad j \in \{w, i, m\} \tag{9}$$

where k_j is the thermal conductivity of the phase j.

The Stefan condition (8) requires the assessment of the normal Lagrangian velocity $v_{\Gamma_{wi}}$. Its determination is clarified below.

2.3. Motion of phase boundary

The phase interface Γ_{wi} is driven by the temperature difference between the equilibrium ice melting point T_M and the current temperature of a given point on Γ_{wi} known as the undercooling (see [40,42,43] for details). The corresponding motion law for Γ_{wi} has the dissipative form relating the normal velocity of an interface point to the mean curvature κ of Γ_{wi} and the undercooling

$$\alpha\gamma v_{\Gamma_{wi}} = -\gamma\kappa + \frac{\varrho_i l_m}{T_M}(T_M - T), \text{ on } \Gamma_{wi} \tag{10}$$

and is known as the Gibbs–Thomson equation. Its derivation assuming the effects of the pressure and the interfacial entropy is presented in [40,44]. Here, $\alpha = \alpha(\mathbf{n}_w)$ is the kinetic coefficient, $\gamma = \gamma(\mathbf{n}_w)$ is the surface tension, both anisotropic, depending on the crystallographic orientation. Due to comparable curvatures of pores and crystals, the anisotropy of growing ice (see, e.g. [45]) has limited space to develop. Despite of that, it is included in the model using the approach of [46].

The motion law (10) itself has been widely treated in literature aiming at its mathematical properties (e.g. in [47]) and algorithms for its numerical solution. These methods rely on direct interface tracking [48,49], or parametric description [50–52], or the level set evolution [53]. In the context of the complex geometry of a porous structure, we use the phase-field method to track the nucleation and growth of particular crystals assuming a diffuse character of Γ_{wi} as described below.

The motion of Γ_{wi} is augmented by the expansion of the ice phase due to the increase of specific volume. This effect is captured by the Lagrangian coordinates and the stress-saturation tensor

$$\alpha_S \frac{E_i}{3(1-2\nu_i)} \hat{I} \tag{11}$$

added to the elastic stress tensor of the water–ice system in agreement with [12,26]. Here, α_S is the coefficient of volumetric expansion due to the phase transition.

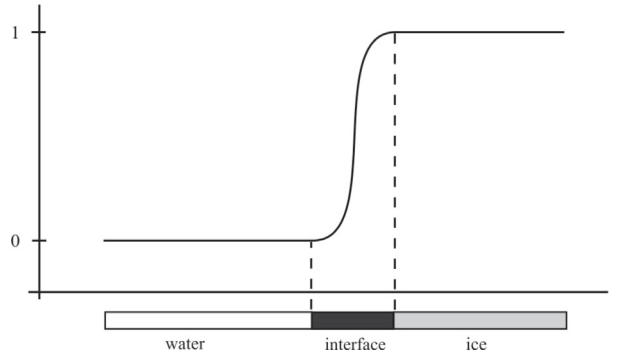

Fig. 2. Illustration of the typical profile of the function w across the solid (ice) and liquid (water) phases.

2.4. Cahn–Hilliard theory of diffuse interfaces

The geometric complexity of the porous structure through which the solid phase of ice grows or vanishes requires a reliable and stable method for tracking the position of the ice crystals at each time moment and at any space position. Such properties are brought by the phase-field method which generates a regularized characteristic function for the position of the phases also known as the order parameter $w = w(\mathbf{X}, t)$ being 0 at one phase (water), 1 at the other phase (ice) and varying smoothly between them across a narrow band of thickness ξ surrounding Γ_{wi} which is identified by the value $w = \frac{1}{2}$ (see Fig. 2). The method is based on the Cahn-Hilliard theory of phase transitions [54,55]. Such an approach has been widely used in the context of solidification modeling, fluid flow, and crystal growth [27,31,33,56–58]. The mentioned theory derives a parabolic nonlinear partial differential equation — the Allen–Cahn equation for the order parameter w

$$\alpha(\nabla w)\gamma\xi^2\partial_t w = \gamma(\nabla w)\xi^2\Delta w + f_0(w) + \xi^2|\nabla w|\frac{\varrho_i l_m}{T_M}(T_M - T), \tag{12}$$

with $f_0(w) = w(1-w)(w-\frac{1}{2})$, in the form suggested in [33]. The equation alone or coupled to the heat conduction equation has been thoroughly studied in the literature (see e.g. [30,33,46,59]). It has been shown employing the matched asymptotics [33,56] that for $\xi \to 0$, the Stefan condition (8) and the Gibbs–Thomson law (10) are recovered at Γ_{wi}:

$$\begin{array}{rcccl} \alpha\gamma\xi\partial_t w & = & \gamma\xi\Delta w + \frac{1}{\xi}f_0(w) & + & \xi|\nabla w|\frac{\varrho_i l_m}{T_M}(T_M - T) \\ \downarrow & & \downarrow & & \downarrow \\ & \xi\to 0 & & & \\ \alpha\gamma v_{\Gamma_{wi}} & = & \gamma\kappa & + & \frac{\varrho_i l_m}{T_M}(T_M - T) \end{array}$$

2.5. Governing equations and boundary conditions

The phase field method allows us to unite the evolving water and ice subdomains and their interface into the pore domain Ω_p. Correspondingly, the equation system is operating the pore domain Ω_p and on the grain domain Ω_m as illustrated in Fig. 3.

The governing system of evolution equations is summarized for $t \in (0, t_{\text{Fin}})$ as

$$\begin{aligned} &\varrho_m c_m \partial_t T = \nabla\cdot(k_m\nabla T), \quad \text{in } \Omega_m, \\ &(w\varrho_i c_i + (1-w)\varrho_w c_w)\partial_t T = \nabla\cdot(wk_i + (1-w)k_w)\nabla T + \varrho_i l_m \partial_t w, \quad \text{in } \Omega_p, \\ &\alpha\xi^2\partial_t w = \gamma\xi^2\Delta w + f_0(w) + \xi^2|\nabla w|\frac{\varrho_i l_m}{T_M}(T_M - T), \quad \text{in } \Omega_p, \end{aligned}$$

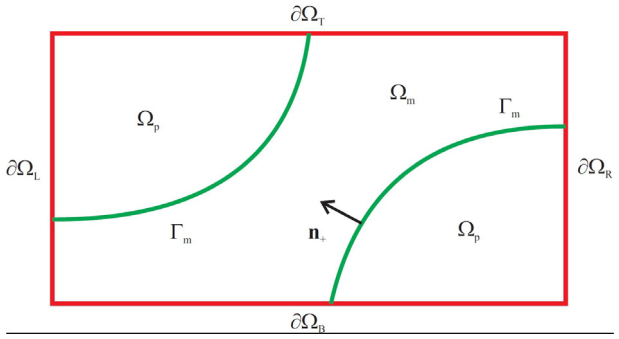

Fig. 3. Illustration of a domain with the parts Ω_p and Ω_m divided by the interface Γ_m. The unit vector $\mathbf{n}_+$ normal to Γ_m points out of Ω_p.

$$
\begin{aligned}
&\varrho_m \frac{\partial^2 \mathbf{u}_m}{\partial t^2} = \nabla \cdot \boldsymbol{\sigma}_m, \quad \text{in } \Omega_m, \\
&(w\varrho_i + (1-w)\varrho_w)\frac{\partial^2 \mathbf{u}_p}{\partial t^2} = \nabla \cdot \boldsymbol{\sigma}_p, \quad \text{in } \Omega_p, \\
&(1-w)\left(\frac{p}{\varrho_w E_w} + \nabla \cdot \mathbf{u}_p\right) = 0, \quad \text{in } \Omega_p.
\end{aligned} \tag{13}
$$

It is accompanied by the constitutive relations

$$
\begin{aligned}
\boldsymbol{\sigma}_m &= \frac{E_m}{1+\nu_m}\hat{e}(\mathbf{u}_m) + \frac{\nu_m E_m \nabla \cdot \mathbf{u}_m}{(1+\nu_m)(1-2\nu_m)}\hat{I}, \\
\boldsymbol{\sigma}_i &= \frac{E_i}{1+\nu_i}\hat{e}(\mathbf{u}_p) + \frac{\nu_i E_i \nabla \cdot \mathbf{u}_p}{(1+\nu_p)(1-2\nu_i)}\hat{I}, \\
\boldsymbol{\sigma}_w &= -p\hat{I} + \mu\partial_t(\nabla \mathbf{u}_p + (\nabla \mathbf{u}_p)^T), \\
\boldsymbol{\sigma}_p &= w\boldsymbol{\sigma}_i + (1-w)\boldsymbol{\sigma}_w + w\alpha_S \frac{E_i}{3(1-2\nu_i)}\hat{I}.
\end{aligned} \tag{14}
$$

The temperature, displacement, and forces are coupled across the boundary Γ_m as

$$
\begin{aligned}
&T|_m = T|_p, \quad \mathbf{n}_+ \cdot (k_m \nabla T)|_m = \mathbf{n}_+ \cdot (wk_i + (1-w)k_w)\nabla T)|_p, \\
&\mathbf{u}_m|_m = \mathbf{u}_p|_p, \quad \mathbf{n}_+ \cdot \boldsymbol{\sigma}_m|_m = \mathbf{n}_+ \cdot \boldsymbol{\sigma}_p|_p.
\end{aligned} \tag{15}
$$

The boundary conditions provide the heat-flux $\mathbf{q}_{out}$ for the energy equation, water phase at the pore edges, and the displacement-free boundary $\partial\Omega_T$

$$
\begin{aligned}
&\mathbf{n}_{\partial\Omega_J \cap \bar{\Omega}_m} \cdot (k_m \nabla T)|_m = \mathbf{q}_{out}, \ \mathbf{n}_{\partial\Omega_J \cap \bar{\Omega}_p} \cdot (k_p \nabla T)|_m = \mathbf{q}_{out}, \\
&\qquad\qquad\qquad\qquad\qquad\qquad\qquad\qquad \text{for } J = B, L, R, T, \\
&\boldsymbol{\sigma}_m \cdot \mathbf{n}_{\partial\Omega_T \cap \bar{\Omega}_m} = \boldsymbol{\sigma}_p \cdot \mathbf{n}_{\partial\Omega_T \cap \bar{\Omega}_m} = 0, \\
&\mathbf{n}^{\perp}_{\partial\Omega_J \cap \bar{\Omega}_m} \cdot (\boldsymbol{\sigma}_m \cdot \mathbf{n}_{\partial\Omega_J \cap \bar{\Omega}_m}) = 0, \ \mathbf{u}_m \cdot \mathbf{n}_{\partial\Omega_J \cap \bar{\Omega}_m}) = 0, \quad \text{for } J = B, L, R, \\
&\mathbf{n}^{\perp}_{\partial\Omega_J \cap \bar{\Omega}_p} \cdot (\boldsymbol{\sigma}_p \cdot \mathbf{n}_{\partial\Omega_J \cap \bar{\Omega}_p}) = 0, \ \mathbf{u}_p \cdot \mathbf{n}_{\partial\Omega_J \cap \bar{\Omega}_p}) = 0, \quad \text{for } J = B, L, R, \\
&w|_{\partial\Omega_p} = 0,
\end{aligned} \tag{16}
$$

where the symbol $\perp$ means the tangent to the boundary. The last boundary condition in (16), for w, reflects the fact that along grains in a porous medium, a water film always persists (see, e.g. [17]). Due to the nature of Eq. (12), in case ice approaches grain, the remaining transition layer has a thickness of the order of ξ. The initial conditions are

$$
\begin{aligned}
&T|_{t=0} = T_{ini}, \quad w|_{t=0} = w_{ini}, \\
&\mathbf{u}_m|_{t=0} = \mathbf{u}_{m,0,ini}, \quad \partial_t \mathbf{u}_m|_{t=0} = \mathbf{u}_{m,1,ini}, \\
&\mathbf{u}_p|_{t=0} = \mathbf{u}_{p,0,ini}, \quad \partial_t \mathbf{u}_p|_{t=0} = \mathbf{u}_{p,1,ini}.
\end{aligned} \tag{17}
$$

The above conditions are adjusted in Section 2 for each of the computational examples. From the solution of this system, the phase interface is identified as $w = \frac{1}{2}$.

3. Computational studies

The model (13)–(17) described above and summarized in Section 2.5 is solved in two-dimensional domains representing vertical cuts of a porous medium.

3.1. Numerical solution

For the numerical solution, the space discretization is performed by the finite element method on a vertically oriented domain $\Omega \subset \mathbb{R}^2$ sketched in Fig. 3 divided by the boundary Γ_m into the pore subdomain Ω_p and the grain matrix subdomain Ω_m, and on a time interval $(0, t_{\text{Fin}})$.

The system of governing Eqs. (13)–(17) is weakly formulated using the test functions

- $v_{T_m} \in H^1(\Omega_m)$, $v_{T_p} \in H^1(\Omega_p)$,
- $v_w \in V_w = \{v \in H^1(\Omega_p) |\ v|_{\partial\Omega_p} = 0\}$,
- $\mathbf{v}_{\mathbf{u}_m} \in V_{\mathbf{u}_m} = \{\mathbf{v} \in H^1(\Omega_m; \mathbb{R}^2) |\ \mathbf{v} \cdot \mathbf{n}_{\partial\Omega_J \cap \bar{\Omega}_m} = 0,\ J = B, L, R\}$,
- $\mathbf{v}_{\mathbf{u}_p} \in V_{\mathbf{u}_p} = \{\mathbf{v} \in H^1(\Omega_p; \mathbb{R}^2) |\ \mathbf{v} \cdot \mathbf{n}_{\partial\Omega_J \cap \bar{\Omega}_p} = 0,\ J = B, L, R\}$,
- $v_p \in V_p = L^2(\Omega_p)$,

and is represented by the following set of weak identities:

$$
\begin{aligned}
&\int_{\Omega_m} \varrho_s c_s \partial_t T v_{T_m} + k_s \nabla T \cdot \nabla v_{T_m} \mathrm{d}x + \int_{\partial\Omega} \mathbf{q}_{out} v_{T_m} \mathrm{d}S \\
&\qquad + \int_{\Gamma_+} (w k_i + (1-w) k_w) \nabla T \cdot \mathbf{n}_+ v_{T_m} \mathrm{d}S = 0, \\
&\int_{\Omega_p} (w\varrho_i c_i + (1-w)\varrho_w c_w) \partial_t T v_{T_p} + (w k_i + (1-w) k_w) \nabla T \cdot \nabla v_{T_p} \mathrm{d}x \\
&\qquad - \int_{\Omega_p} \varrho_i l_m \partial_t w v_{T_p} \mathrm{d}x + \int_{\partial\Omega} \mathbf{q}_{out} v_{T_p} \mathrm{d}S - \int_{\Gamma_+} k_p \nabla T \cdot \mathbf{n}_+ v_{T_p} \mathrm{d}S = 0, \\
&\int_{\Omega_p} \alpha \xi^2 \partial_t w v_w + \gamma \xi^2 \nabla w \cdot \nabla v_w + f_0(w) v_w + \xi^2 |\nabla w| \frac{\varrho_i l_m}{T_M} (T_M - T) v_w \mathrm{d}x = 0, \\
&\int_{\Omega_m} \varrho_m \frac{\partial^2 \mathbf{u}_m}{\partial t^2} \cdot \mathbf{v}_m + \boldsymbol{\sigma}_m : \nabla \mathbf{v}_m \mathrm{d}x + \int_{\Gamma_m} \boldsymbol{\sigma}_p \mathbf{n}_+ \cdot \mathbf{v}_m \mathrm{d}S = 0, \\
&\int_{\Omega_p} (w\varrho_i + (1-w)\varrho_w) \frac{\partial^2 \mathbf{u}_p}{\partial t^2} \cdot \mathbf{v}_p + \boldsymbol{\sigma}_p : \nabla \mathbf{v}_p) \mathrm{d}x - \int_{\Gamma_m} \boldsymbol{\sigma}_m \mathbf{n}_+ \cdot \mathbf{v}_p \mathrm{d}S = 0, \\
&\int_{\Omega_p} (1-w) \left(\frac{p}{\varrho_w E_w} v_p + \nabla \cdot \mathbf{u}_p \cdot v_p \right) \mathrm{d}x = 0.
\end{aligned}
\tag{18}
$$

The numerical solution is obtained through the Faedo–Galerkin approximation of (18) (see, e.g. [60]) based on the triangulations $\mathcal{T}_p$ of Ω_p and $\mathcal{T}_m$ of Ω_m consisting of the triangular Lagrange elements of the second order. The semi-discrete scheme consisting of ordinary differential equations is solved by the generalized α-method which is implicit and second-order accurate (see [61]). In the pore subdomains, the diameter of elements is limited by the phase-field small parameter ξ as indicated in the description of each computation. This guarantees proper behavior of the Allen–Cahn equation in the form (12) as discussed in [33,46,59]. The algorithmic realization of the scheme has been operated in the software Comsol.

3.2. Computational examples

The following computational examples describe the behavior of the model reflecting the ice phase growth inside a pore structure, interaction with the grain structure, universal positioning of the solid phase in pores and expansion of the medium due to the difference in density of the ice and water phases.

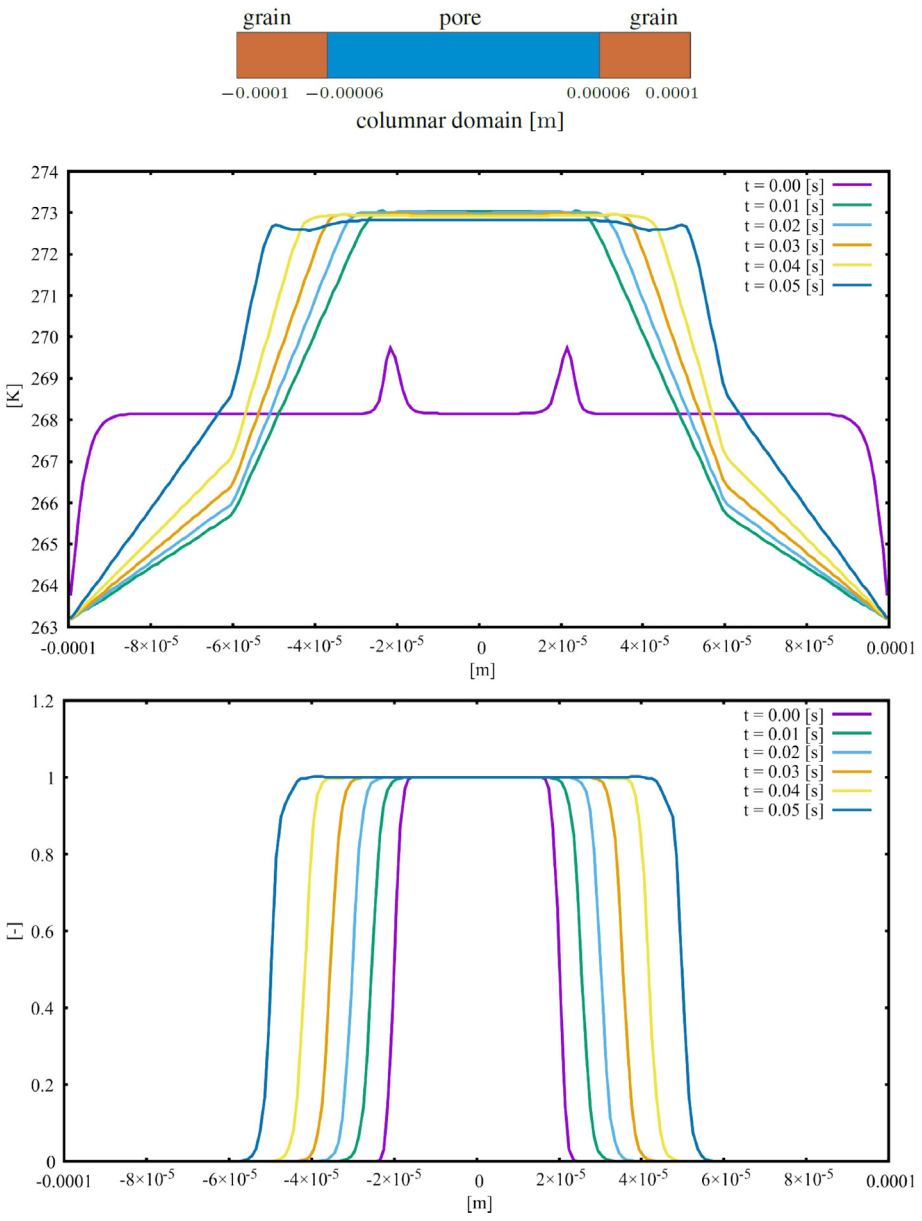

Fig. 4. Computation 1: Temperature and ice phase evolution in a one-dimensional micro-pore (scale in m). The solid phase gradually grows in the pore filled with the liquid phase. Due to different heat capacities and conductivities in water and grain, the temperature has different slopes in the pore and the grains.

The setup of key physical quantities is summarized in Table 1. For porous medium mass and heat parameters, see [62,63], ice properties are summarized, e.g. in [64], surface tension parameters in [65–67], and kinetics of crystal growth in [68]. The phase diffuse interface layer is indicated by a couple of isolines $w = 0.4, 0.6$. The two-dimensional ice anisotropy in (12) is, for simplicity, chosen as $\alpha_0/\alpha = \sigma_0/\sigma = 1 + 0.7\cos(6\theta(\nabla w))$ where $\theta(\nabla w)$ is the angle between the crystallographic orientation (e.g. set as $\pi/8$ in our computational examples) and the vector $\mathbf{n}_w$. For some details and complexity of ice crystals, see e.g. [49].

Computation 1. This study is computed on the domain shown in Fig. 4 above. It shows a one-dimensional columnar symmetric porous structure where solidification occurs in the pore without considering the volumic expansion. The

Table 1
Values of physical parameters.

Symbol	Value	Symbol	Value	Symbol	Value
c_w	4.2 [kJ/(kg K)]	c_i	2.1 [kJ/(kg K)]	c_m	1 [kJ/(kg K)]
ξ	$\sim 10^{-8}$ [m]	E_w	5.33 [GPa]	E_i	7.8 [GPa]
E_m	75 [GPa]	h	0.3 [μm]	k_w	0.6 [W/(m K)]
k_i	0.6 [W/(m K)]	k_m	0.6 [W/(m K)]	l_{m}	334 [kJ/kg]
μ	180 [Pa s]	ν_i	0.33 [1]	ν_m	0.33 [1]
q	100 [W/m]	r	3 [μm]	ϱ_w	1000 [kg m^{-3}]
ϱ_i	920 [kg m^{-3}]	ϱ_m	2500 [kg m^{-3}]	α_s	0.13 [GPa]
α_0	1.85×10^{-7} [s m^{-2}]	γ_0	0.033 [J m^{-2}]	ζ	0.5 [1]

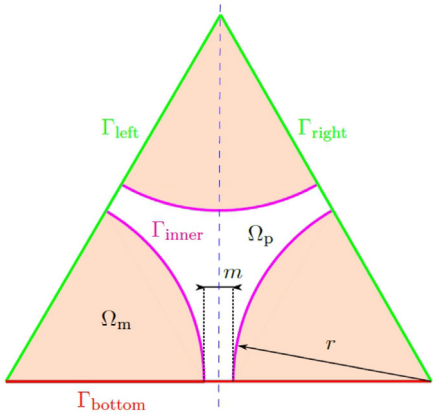

Fig. 5. Illustration of the triangular domain representing a vertical cut of a regular porous structure with the particle radius $r = 2.8$ μm and particle distance $m = 0.9$ μm.

initial temperature was $T_{ini} = 268.15$ K, the boundary temperature at both ends was 263.15 K, the nucleation diameter was 40 μm, and the phase-field parameter is $\xi = 8 \times 10^{-7}$ m. Ice grows driven by undercooling as shown in Fig. 4 with the spatial profile of the phase function $w = w(t, x)$ evolving in time, correspondingly.

Computation 2. This study has been computed on the domain described in Fig. 5. It shows the phenomenon of coalescence (merging two growing phases) well known in material science [69]. The process is driven by heat exchange. The computation does not consider structural changes. The phase function has the zero Dirichlet boundary condition, the Newton heat flux of $\mathbf{q}_{out} = 30(272.15 - T)$ W m^{-2} is on Γ_{left} and Γ_{right}, and isolation is on Γ_{bottom}. The initial temperature is 273.10 K, nucleation radii are 0.3 μm, the phase-field parameter is $\xi = 5 \times 10^{-8}$ m, and the maximum element diameter in the pore is 0.10 μm. As a result of the time evolution, both ice crystals merge and occupy the position centered within the pore as shown in Fig. 6.

Computation 3. This computation has been performed on the domain described in Fig. 7 with zero normal displacement at the domain edges, zero Dirichlet boundary condition for the phase function and the Newton heat flux $\mathbf{q}_{out} = 30(272.15 - T)$ W m^{-2} along the upper edge of the boundary, isolation along other boundary edges. The initial temperature is 272.2 K, the nucleation radius is 0.3 μm, and the phase-field parameter is $\xi = 8 \times 10^{-8}$ m, the maximum element diameter in the pore is 0.12 μm. This study compares the phase transformation and structural dynamics for three different positions of the nucleation site (a), (b), and (c). As a result of the time evolution in the pore geometry, ice always occupies the position centered within the largest part of the pore as shown in the third row of Fig. 8.

Computation 4. Using the same domain described in Fig. 7 with zero normal displacement at the domain boundary, zero Neumann boundary condition for the phase function, and the Newton heat flux $\mathbf{q}_{out} = 300(270.65 - T)$ W m^{-2}

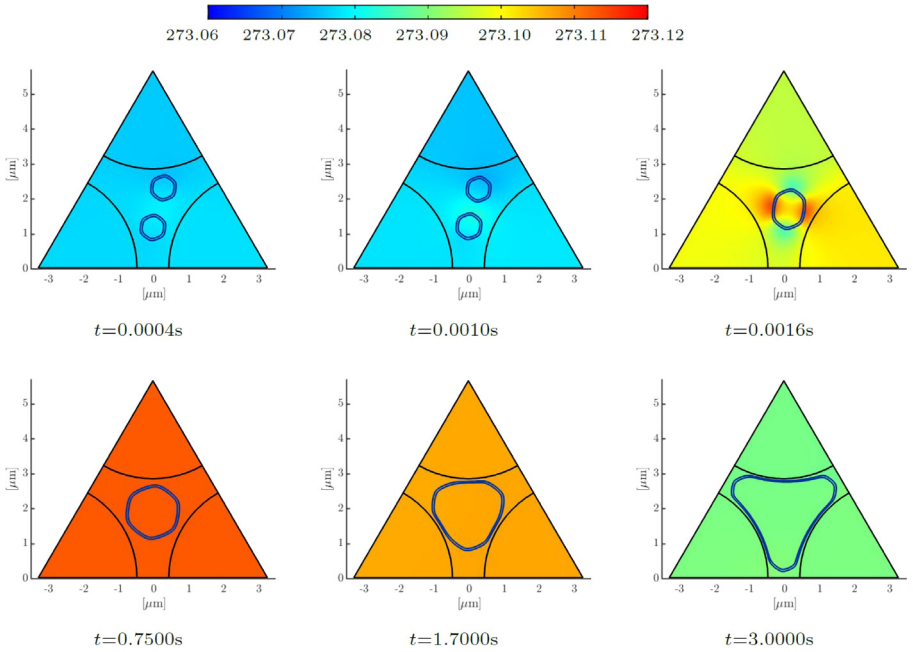

Fig. 6. Computation 2: Temperature distribution and solid phase evolution in a symmetric trifold micro-pore (scale in μm). Two ice crystals coalesce and create a single pattern centered in the pore. A thin diffuse interface remains between ice and grains.

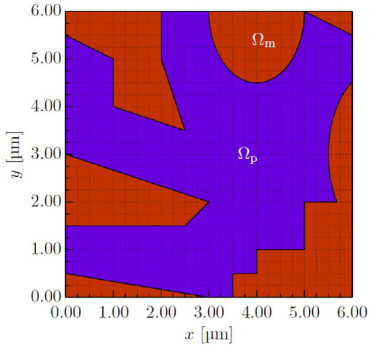

Fig. 7. The domain represents a vertical cut of a pore structure for Computation 3, 4 and 6. The grains are in red and pore in blue. (For interpretation of the references to color in this figure legend, the reader is referred to the web version of this article.)

along the upper edge of the boundary, isolation along other boundary edges, the solidification dynamics is initiated by a single nucleation site of radius 0.3 μm placed at the boundary. The initial temperature is $T_{ini} = 272.15$ K. The phase-field small parameter $\xi = 8 \times 10^{-8}$ m, the maximum element diameter in the pore is 0.12 μm. As a result, one can observe that ice grows from the boundary and fills the entire volume in a way similar to Computation 3 - see Fig. 9 - but faster due to different thermal circumstances.

Computation 5. In a general porous structure within the domain described in Fig. 10 with zero normal displacement at the domain right and bottom edges and free displacement at the domain top and left edges, zero Dirichlet boundary condition for the phase function, and the heat flux 50 W m^{-2} for $t > 0.5$ s along the entire boundary, the solidification dynamics is initiated by two nucleation sites of radius 10 μm. The initial temperature is $T_{ini} = 273.15$ K. The phase-field small parameter $\xi = 8 \times 10^{-6}$ m, and the maximum element diameter in the pore domain is

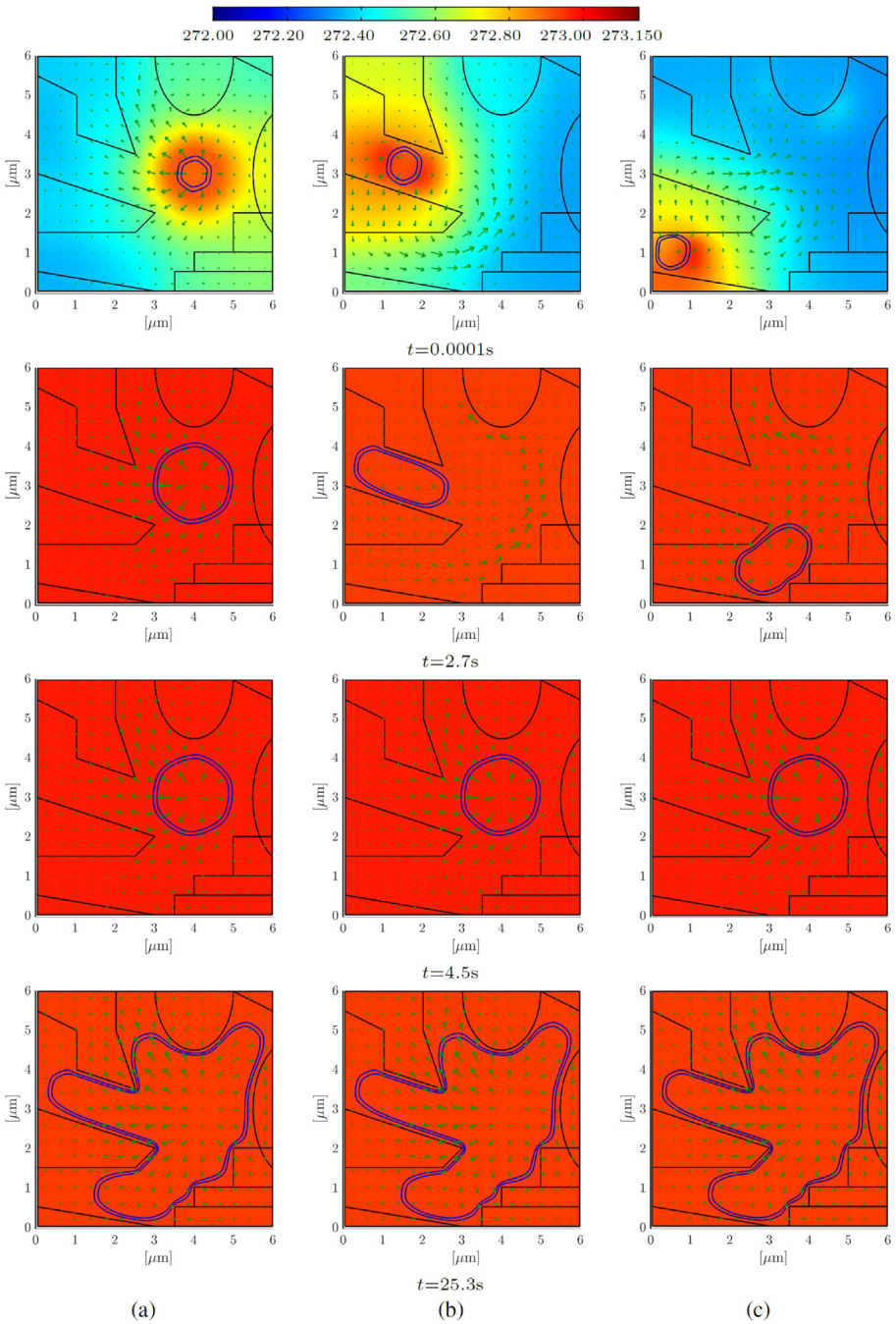

Fig. 8. Computation 3: Comparison of temperature, solid phase, and displacement evolution in a general pore for different positions of the nucleus. The temperature is in a color scale, the phase boundary is indicated by a double isoline of w, and the displacement is indicated by green arrows of proportional length. (For interpretation of the references to color in this figure legend, the reader is referred to the web version of this article.)

7 μm. As a result, one can observe two ice phase areas coexisting due to a larger initial mutual distance. They gradually approach and tend to fill the entire volume which expands due to the difference in specific volumes of phases and free conditions on top and left edges — see Fig. 11.

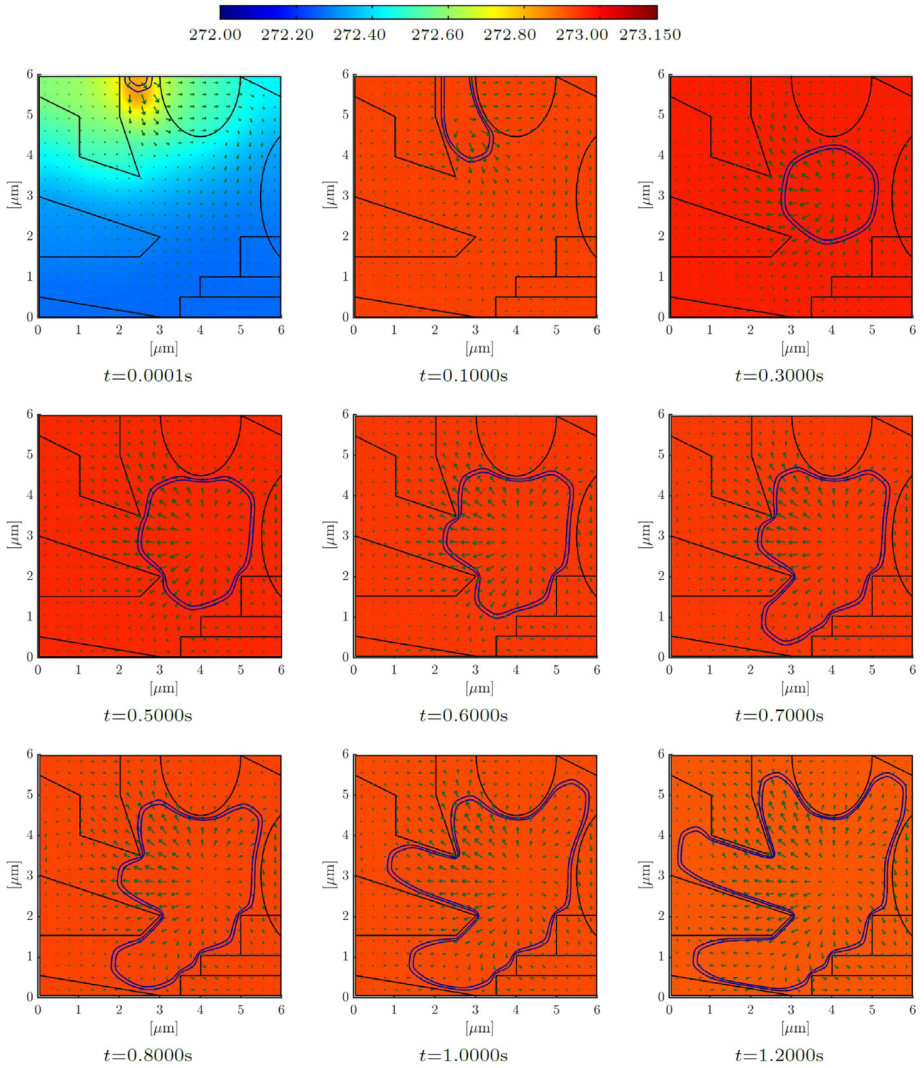

Fig. 9. Computation 4: Evolution of temperature, solid phase, and displacement in a general pore with nucleation at the pore boundary. The temperature is in a color scale, the phase boundary is indicated by a double isoline of w, and the displacement is indicated by green arrows of proportional length. (For interpretation of the references to color in this figure legend, the reader is referred to the web version of this article.)

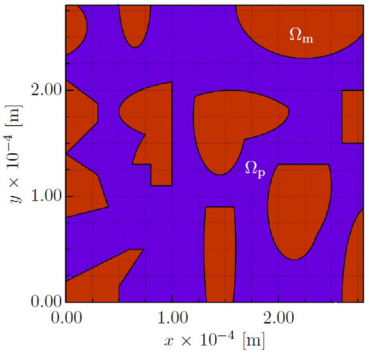

Fig. 10. The domain represents a vertical cut of a pore structure for Computation 5. The grains are in red and pore in blue. (For interpretation of the references to color in this figure legend, the reader is referred to the web version of this article.)

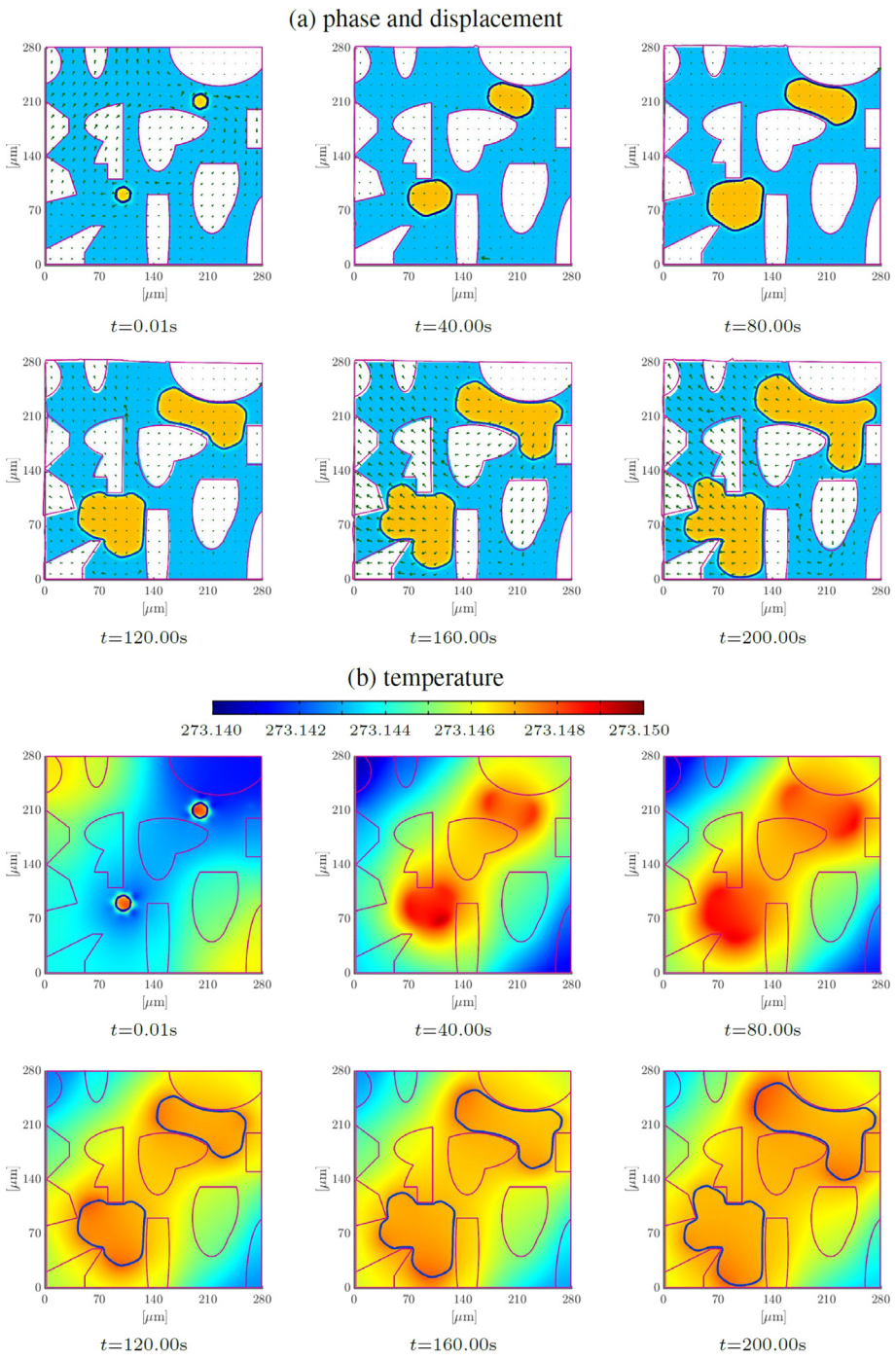

Fig. 11. Computation 5: Showing temperature, ice phase, and displacement dynamics in a small pore of general shape given in Fig. 10. In (a), ice is in yellow, water in light blue, the phase boundary is indicated by a double isoline of w and the displacement is indicated by green arrows of proportional length. The shape deformation is indicated by a violet contour with a scale factor 2. In (b), the temperature field is in a color scale, the phase boundary is indicated by a double isoline of w. The displacement of both matrix and liquid phases through the unconstrained domain boundaries is induced by the change in volume of forming solid phase. (For interpretation of the references to color in this figure legend, the reader is referred to the web version of this article.)

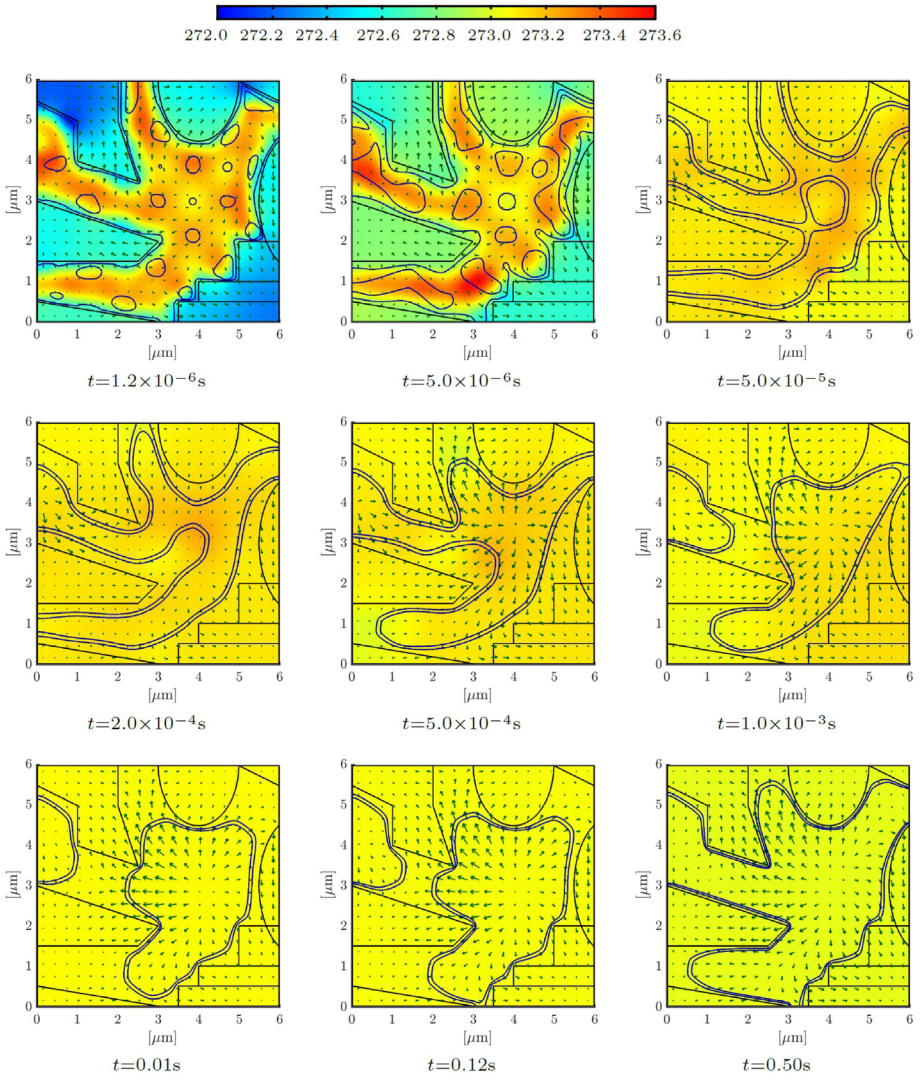

Fig. 12. Computation 6: Evolution of temperature, solid phase, and displacement in a general pore with homogeneous nucleation in the pore volume. The temperature is in a color scale, the phase boundary is indicated by a double isoline of w, and the displacement is indicated by green arrows of proportional length. (For interpretation of the references to color in this figure legend, the reader is referred to the web version of this article.)

Computation 6. Using the domain described in Fig. 7 with zero normal displacement at the domain edges, zero Neumann boundary condition for the phase function and the Newton heat flux $\mathbf{q}_{out} = 300(270.65 - T)$ W m^{-2} along the upper edge of the boundary, isolation along other boundary edges, the initial temperature is $T_{ini} = 272.15$ K. The initial condition for the phase function $w_{ini} = 0.5 + 0.1\cos(8\pi x/6 \times 10^{-6})\cos(8\pi x/6 \times 10^{-6})$ is set as a perturbation of the metastable state $w = 0.5$ to induce a homogeneous nucleation. The phase-field small parameter $\xi = 8 \times 10^{-8}$ m, and the maximum element diameter in the pore is 0.12 μm. As a consequence of the initial condition, ice nucleates spontaneously at various positions in the pore, grows, and fills the pore — see Fig. 12.

4. Conclusion

The model of solidification in a porous medium at the pore scale has been formulated by using the conservation laws of mass, momentum, and energy. The phase dynamics is tracked through the anisotropic Allen–Cahn equation which is coupled to the momentum evolution law. The model is able to describe the ice-phase expansion which

induces the structural dynamics in the entire volume of the porous structure. It can serve for describing the onset of the water–ice phase transition with mechanical effects in the pore structure.

The presented computational studies are two-dimensional. However, the model can be used in three-dimensional pore geometry without any restriction, just with higher CPU costs. Further development of the model should be directed to the interfacial phenomena between ice and grain matrix where specific transport phenomena have been noticed in literature.

Declaration of competing interest

The authors declare that they have no known competing financial interests or personal relationships that could have appeared to influence the work reported in this paper.

Data availability

No data was used for the research described in the article.

Acknowledgments

The authors were partly supported by the project of the Czech Ministry of Education, Youth and Sports Interexcellence LTAUSA19021 and by the project 21-09093S of the Czech Science Foundation.

References

[1] G. Beskow, Soil freezing and frost heaving with special application to roads and railroads, 1935, The Swedish Geological Society, C, (375) Year Book no.3 (Translated by J.O. Osterberg), Reprinted 1991 CRREL Spec. Rep..
[2] G.L. Guymon, R.L. Berg, T.V. Hromadka, Mathematical Model of Frost Heave and Thaw Settlement in Pavements, CRREL Rep. 93-2, Hanover, 1993.
[3] L.C. Lundin, Water and heat flows in frozen soils, Basic theory and operational modeling (Ph.D. thesis), Uppsala University, Uppsala, 1989.
[4] J. Wilkerson, How much worse will thawing arctic permafrost make climate change? Sci. Am. (2021).
[5] J. Li, Y. Luo, S. Natali, E. Schuur, J. Xia, E. Kowacyk, Y. Wang, Modeling permafrost thaw and ecosystem carbon cycle under annual and seasonal warming at an arctic tundra site in Alaska, J. Geophys. Res. Biogeosci. 119 (6) (2014) 1129–1146.
[6] S. Taber, The mechanics of frost heaving, J. Geol. 38 (1930) 303–317.
[7] A.W. Skempton, Effective stress in soils, in: Concrete and Rocks, Thomas Telford Publishing, 1961, pp. 106–118.
[8] R.D. Miller, Frost heaving in non-colloidal soils, in: Proc. 3rd Int. Conference on Permafrost, Edmonton, 1978.
[9] J. Hartikainen, M. Mikkola, Thermomechanical model of freezing soil by use of the theory of mixtures, in: Proc. of the 6th Finnish Mechanics Days, Oulu, 1997.
[10] O. Coussy, Poromechanics, Wiley, New York, 2004.
[11] S. Nishimura, A. Gens, S. Olivella, R.J. Jardine, Thm-coupled finite element analysis of frozen soil: formulation and application, Gé 59 (3) (2009) 159–171.
[12] O. Coussy, Poromechanics of freezing materials, J. Mech. Phys. Solids 53 (2005) 1689–1718.
[13] N. Li, F. Chen, B. Xu, G. Swoboda, Theoretical modeling framework for an unsaturated freezing soil, Cold Reg. Sci. & Technol. 54 (2008) 19–35.
[14] A. Gens, Soil-environment interactions in geotechnical engineering, Géotechnique 60 (1) (2010) 3–74.
[15] M. Frémond, P. Nicolas, Macroscopic thermodynamics of porous media, Contin. Mech. Thermodyn. 2 (1990) 119–139.
[16] A.W. Rempel, J.S. Wettlaufer, M.G. Worster, Premelting dynamics in a continuum model of frost heave, J. Fluid Mech. 498 (2004) 227–244.
[17] A.W. Rempel, Microscopic and environmental controls on the spacing and thickness of segregated ice lenses, Quat. Res. 75 (2011) 316–324.
[18] A.H. Sweidan, Y. Heider, B. Markert, A unified water/ice kinematics approach for phase-field thermo-hydro-mechanical modeling of frost action in porous media, Comput. Methods Appl. Mech. Eng. 372 (2020) 113358.
[19] A.H. Sweidan, K. Niggemann, Y. Heider, M. Ziegler, B. Markert, Experimental study and numerical modeling of the thermo-hydro-mechanical processes in soil freezing with different frost penetration directions, Acta Geotech. 17 (2022) 231–255.
[20] H.S. Suh, W.C. Sun, Multi-phase-field microporomechanics model for simulating ice-lens growth in frozen soil, Int. J. Numer. Anal. Methods Geomech. 46 (12) (2022) 2307–2336.
[21] M. Mikkola, J. Hartikainen, Mathematical model of soil freezing and its numerical implementation, J. Numer. Methods Eng. 52 (2001) 543–557.
[22] J.F. Nixon, N.R. Morgenstern, The residual stress in thawing soils, Can. Geotech. J. 10 (4) (1973) 571–580.
[23] M. Furuzumi, Y. Takeshita, M. Kurashige, F. Nishimura, K. Hirose, K. Imai, Thermal and freezing strains on a face of wet sandstone samples under a subzero temperature cycle, J. Therm. Stresses 27 (2004) 331–344.

[24] A. Žák, M. Beneš, T.H. Illangasekare, Analysis of model of soil freezing and thawing, IAENG Int. J. Appl. Math. 43 (3) (2013) 127–134.
[25] A. Žák, M. Beneš, T.H. Illangasekare, A.C. Trautz, Mathematical model of freezing in a porous medium at micro-scale, Commun. Comput. Phys. 24 (2) (2018) 557–575.
[26] A. Žák, M. Beneš, Micro-scale model of thermomechanics in solidifying saturated porous media, Acta Phys. Pol. A 134 (3) (2018) 678–682.
[27] P. Strachota, A. Wodecki, M. Beneš, Focusing the latent heat release in 3D phase field simulations of dendritic crystal growth, Model. Simul. Mater. Sci. Eng. 29 (6) (2021) 065009.
[28] P.-A. Geslin, C.-H. Chen, A.M. Tabrizi, A. Karma, Dendritic needle network modeling of the columnar-to-equiaxed transition Part I: Two dimensional formulation and comparison with theory, Acta Mater. 202 (2021) 42–54.
[29] Z. Jia, W. Qi, Y. Xiaofeng, Numerical approximations for a phase field dendritic crystal growth model based on the invariant energy quadratization approach, Internat. J. Numer. Methods Engrg. 110 (2017) 279–300.
[30] M. Beneš, Mathematical and computational aspects of solidification of pure substances, Acta Math. Univ. Comenianae 70 (1) (2001) 123–152.
[31] W.J. Boettinger, A.A. Wheeler, B.T. Murray, G.B. McFadden, Prediction of solute trapping at high solidification rates using a diffuse interface phase-field theory of alloy solidification, Technical report, NIST, 1993, NATO Advanced Research Workshop: Undercooled Metallic Melts: Properties, Solidification and Metastable Phases, Il Ciocco.
[32] A.A. Wheeler, W.J. Boettinger, G.B. McFadden, Phase-field model of solute trapping during solidification, Phys. Rev. E 47 (1993) 1893–1909.
[33] M. Beneš, Mathematical analysis of phase-field equations with numerically efficient coupling terms, Interfaces Free Boundaries 3 (2001) 201–221.
[34] A. Mikelić, M.F. Wheeler, On the interface law between a deformable porous medium containing a viscous fluid and an elastic body, Math. Models Methods Appl. Sci. 22 (2012) 1–32.
[35] M.E. Gurtin, A. Struthers, Multiphase thermomechanics with interfacial structure, Arch. Ration. Mech. Anal. 112 (1990) 97–160.
[36] J.E. Marsden, T.J.R. Hughes, Mathematical Foundations of Elasticity, Dover Publications Inc., New York, 1994.
[37] S. Davis, Interfacial fluid dynamics, in: G.K. Batchelor, H.K. Moffatt, M.G. Worster (Eds.), Perspectives in Fluid Dynamics (A Collective Introduction to Current Research), Cambridge, 2003, pp. 1–52.
[38] M.G. Worster, Solidification of fluids, in: G.K. Batchelor, H.K. Moffatt, M.G. Worster (Eds.), Perspectives in Fluid Dynamics (A Collective Introduction to Current Research), pages 393–446, Cambridge, 2003.
[39] H. Garcke, B. Nestler, B. Stoth, A multiphase field concept: Numerical simulations of moving phase boundaries and multiple junctions, SIAM J. Appl. Math. 60 (1) (1999) 295–315.
[40] M.E. Gurtin, On the two-phase stefan problem with interfacial energy and entropy, Arch. Ration. Mech. Anal. 96 (3) (1986) 199–241.
[41] A. Visintin, Models of Phase Transitions, Birkhäuser, Boston, 1996.
[42] M. Gurtin, On the two-phase stefan problem with interfacial energy and entropy, Arch. Ration. Mech. Anal. 96 (1986) 200–240.
[43] M. Gurtin, Thermomechanics of Evolving Phase Boundaries in the Plane, Clarendon Press, Oxford, 1993.
[44] J.R. King, J.D. Evans, Regularization by kinetic undercooling of blow-up in the ill-posed stefan problem, SIAM J. Appl. Math. 65 (5) (2005) 1677–1707.
[45] Y. Teraoka, A. Saito, S. Okawa, Study on anisotropy of growth rate of ice crystal in supercooled water, Int. J. Refrig. 27 (3) (2004) 242–247.
[46] M. Beneš, Diffuse-interface treatment of the anisotropic mean-curvature flow, Appl. Math. 48 (6) (2003) 437–453.
[47] K. Deckelnick, Weak solutions of the curve shortening flow, Calc. Var. Partial Differential Equations 5 (6) (1997) 489–510.
[48] A. Schmidt, Computation of three dimensional dendrites with finite elements, J. Comput. Phys. 125 (2) (1996) 293–312.
[49] E. Yokoyama, T. Kuroda, Pattern formation in growth of snow crystals occurring in the surface kinetics process and the diffusion process, Phys. Rev. A 41 (1990) 2038–2049.
[50] K. Deckelnick, G. Dziuk, Discrete anisotropic curvature flow of graphs, ESAIM Math. Model. Numer. Anal. 33 (06) (1999) 1203–1222.
[51] V. Minárik, J. Kratochvíl, K. Mikula, M. Beneš, Numerical simulation of dislocation dynamics, in: M. Feistauer, V. Dolejší, P. Knobloch, K. Najzar (Eds.), Numerical Mathematics and Advanced Applications, ENUMATH 2003 (peer reviewed proceedings), pages 631–641, Berlin, 2003, pp. 631–641.
[52] V. Minárik, M. Beneš, J. Kratochvíl, Simulation of dynamical interaction between dislocations and dipolar loops, J. Appl. Phys. 107 (2010) 061802.
[53] M. Beneš, K. Mikula, T. Oberhuber, D. Ševčovič, Comparison study for level set and direct Lagrangian methods for computing Willmore flow of closed planar curves, Comput. Vis. Sci. 12 (2009) 307–317.
[54] J.W. Cahn, J.E. Hilliard, Free energy of a nonuniform system I. Interfacial free energy, J. Chem. Phys. 28 (1958) 258–267.
[55] S. Allen, J. Cahn, A microscopic theory for antiphase boundary motion and its application to antiphase domain coarsening, Acta Metall. 27 (1979) 1084–1095.
[56] G. Caginalp, An analysis of a phase field model of a free boundary, Arch. Ration. Mech. Anal. 92 (1986) 205–245.
[57] R. Kobayashi, Modeling and numerical simulations of dendritic crystal growth, Physica D 63 (1993) 410–423.
[58] H.-R. Liu, C. Shen Ng, K. Leong Chong, D. Lohse, R. Verzicco, An efficient phase-field method for turbulent multiphase flows, J. Comput. Phys. 446 (2021) 110659.
[59] M. Beneš, Computational studies of anisotropic diffuse interface model of microstructure formation in solidification, Acta Math. Univ. Comenianae 76 (1) (2009) 35–50.
[60] V. Thomée, Galerkin finite element methods for parabolic problems, in: Springer Series in Computational Mathematics, 25, New York, 2006.

[61] J. Chung, G.M. Hulbert, A time integration algorithm for structural dynamics with improved numerical dissipation: The generalized-α method, J. Appl. Mech. 60 (2) (1993) 371–375.
[62] J.J. Kumara, Y. Kikuchi, T. Kurashina, Effective length of the soil plug of inner-sleeved open-ended piles in sand, J. GeoEng. 10 (3) (2015) 75–82.
[63] H. Kiyohashi, S. Sasaki, H. Masuda, Effective thermal conductivity of silica sand as a filling material for crevices around radioactive-waste canisters, High Temp. High Pressures 35/36 (2003/2004) 179–192.
[64] Y.-C. Yen, Review of thermal properties of snow, ice and sea ice, in: Technical Report CRREL Report 81-10, U.S. Army Corps of Engineers, Cold Regions Research and Engineering Laboratory, Hanover, New Hamphsire, U.S.A, 1981.
[65] P.J. Williams, Use of the ice-water surface tension concept in engineering practice, in: Technical Report Washington District of Columbia, United States, 51st Annual Meeting of the Highway Research Board, 1972.
[66] B.J. Mason, The Physics of Clouds, Clarendon Press, Oxford, 1971.
[67] D.M. Anderson, The interface between ice and silicate surface, Technical Report Research Report 219, U.S. Army Materiel Command, Cold Regions Research and Engineering Laboratory, Hanover, New Hamphsire, U.S.A, 1981.
[68] S.C. Hardy, S.R. Coriell, Surface tension and interface kinetics of ice crystals freezing and melting in sodium chloride solutions, J. Cryst. Growth 20 (1973) 292–300.
[69] W. Kurz, D.J. Fischer, Fundamentals of Solidification, Trans. Tech. Publishers, Aedermannsdorf, 1989.